ORIGINAL PAPER-PRODUCTION ENGINEERING

Construction of pore structure and lithology of digital rock physics based on laboratory experiments

Chenzhi Huang[1] · Xingde Zhang[1] · Shuang Liu[1] · Nianyin Li[2] · Jia Kang[2] · Gang Xiong[1]

Abstract

The development and stimulation of oil and gas fields are inseparable from the experimental analysis of reservoir rocks. Large number of experiments, poor reservoir properties and thin reservoir thickness will lead to insufficient number of cores, which restricts the experimental evaluation effect of cores. Digital rock physics (DRP) can solve these problems well. This paper presents a rapid, simple, and practical method to establish the pore structure and lithology of DRP based on laboratory experiments. First, a core is scanned by computed tomography (CT) scanning technology, and filtering back-projection reconstruction method is used to test the core visualization. Subsequently, three-dimensional median filtering technology is used to eliminate noise signals after scanning, and the maximum interclass variance method is used to segment the rock skeleton and pore. Based on X-ray diffraction technology, the distribution of minerals in the rock core is studied by combining the processed CT scan data. The core pore size distribution is analyzed by the mercury intrusion method, and the core pore size distribution with spatial correlation is constructed by the kriging interpolation method. Based on the analysis of the core particle-size distribution by the screening method, the shape of the rock particle is assumed to be a more practical irregular polyhedron; considering this shape and the mineral distribution, the DRP pore structure and lithology are finally established. The DRP porosity calculated by MATLAB software is 32.4%, and the core porosity measured in a nuclear magnetic resonance experiment is 29.9%; thus, the accuracy of the model is validated. Further, the method of simulating the process of physical and chemical changes by using the digital core is proposed for further study.

Abbreviations

$f(x, y)$	Represents the distribution function of attenuation coefficient of a section of the tested sample
$P(\rho, \theta)$	Expression of projection function of $f(x, y)$ along θ direction
$|\rho|$	Filter function
$g(t, \theta)$	The filtered projection of $P(\rho, \theta)$
ρ	Distance from a point to a pole, μm
t	Abscissa of a point (x, y) on the scanning section of the measured sample in polar coordinate system
ω_1	The proportion of the number of background group pixels in the whole image
ω_2	The proportion of the number of pixels in the target group in the whole image
$\overline{\text{gray}}_1$	Background group average gray
$\overline{\text{gray}}_2$	Average gray level of target group
N	Total number of CT scan pixels
N_{T_i}	The number of pixels with gray value of T_i–T_{i+1}
ω_{m_i}	Mass fraction of a mineral
gray_{T_i}	The gray value is T_i–T_{i+1}
d_i	The maximum particle size of a mineral in the core, μm
d_{P_i}	The size distribution range of a mineral, μm
R	Aperture, μm
θ	Wetting angle, °
λ_i	Undetermined weight coefficient

✉ Chenzhi Huang
huang_chzh@petrochina.com.cn

[1] Research Institute of Natural Gas Technology, Southwest Oil and Gas Field Company, Petrochina, Chengdu 610213, China

[2] State Key Laboratory of Oil and Gas Reservoir Geology and Exploitation Engineering, Southwest Petroleum University, Chengdu 610500, Sichuan, China

n^*	Total number of samples
$N(j - x)$	The total number of sample points when the separation distance is $j - x$
(x_0, y_0, z_0)	Coordinate of descent point
(x_i, y_i, z_i)	Neighborhood coordinates of descent point
d_i	The sum of the distances from the descent point to each point in the neighborhood, μm
d^*	The minimum value of the sum of distances from the descent point to the points in the neighborhood, μm
h_t	Number of intersected blue dotted spheres
V_p	Volume of rock particles, μm^3
V_{rock}	Total volume of rock, μm^3

Introduction

The development of new wells and the stimulation of production of old wells are inseparable from the experimental analysis of reservoir cores. Measures for developing or increasing the number of oil and gas wells are proposed based on the experimental results. Comprehensive and accurate experimental analysis of reservoir cores, such as core sensitivity experiments, conductivity analysis, acid and fracturing fluid damage experiments, are the key to improving the production of these wells (Sadeq et al. 2018; Wan et al. 2011). However, for these experiments, a large number of cores and, in particular, acid and fracturing fluid damage evaluation experiments are necessary (for example, for five types of liquids, five concentrations are considered for each type of liquid additive, and 25 cores are needed) (Fu et al. 2020; Al-Fatlawi et al. 2017). There are many requirements with regard to liquid type or additive concentrations, and in many cases, the sampling cores are not sufficient to complete some necessary experiments. Moreover, if the reservoir is thin, the problem is more serious. The establishment of digital rock physics (DRP) will largely solve the problem of insufficient cores. Experimental analyses are often time consuming. In particular, for low-permeability reservoirs, the core is very dense, and it still takes a long time to complete a set of analysis experiments under high displacement pressure. DRP can greatly reduce the time required for experimental analysis by employing the rapid calculation ability of computers and can reduce the experimental cost and manpower. Considering the huge development potential of digital cores, many researchers were motivated to perform different studies on DRP.

X-ray computed tomography imaging and digital core analyses are being increasingly used to calculate the porosity and permeability from the millimeter to centimeter scale in Earth science. DRP is an effective method for calculating physical properties of rock using high-resolution three-dimensional (3D) images (Karimpouli et al. 2020). DRP technology can characterize the microstructure of rock at the pore scale and

allow a quantitatively study of the relation between rock physical parameters and rock physical properties. Dvorkin et al. (2009) and Kuntz et al. (2000) used digital cores to study various rock physical properties (DRP), including acoustic properties, electrical properties, nuclear magnetic resonance relaxation, and permeability. With the development of CT scanning technology, DRP technology has progressed rapidly. In fact, the 3D pore geometry structures of reservoir rocks can be captured and visualized clearly (Riepe et al. 2011; Kalam et al. 2013). The higher the scanning accuracy, the more accurate is the rock microstructure presented by means of the filtered back-projection reconstruction (Arns et al. 2002). Through a series of image-processing techniques, the digital processing of rock can be implemented and the available pore space, fluid transport properties, and other rock properties, such as elastic modulus, formation resistivity factor, and relative permeability curve, can be quantified (Schembre and Kovscek 2003; Saenger et al. 2004; Taud et al. 2005). Andrä et al. (2013) discussed in detail the segmentation of the gray value of the CT scanning results, compared the segmentation results with four different types of rock samples, and discussed the uncertainty in image segmentation.

Many types of rock digital-processing technologies are available. Mostaghimi et al. (2012) applied an algebraic multigrid method to study the permeability anisotropy at the pore scale and opined that rock pores are mainly unidirectionally connected. Shabro et al. (2012) applied a finite difference method in which a weighting factor is defined and a Laplace equation is solved to study the flow characteristics of the fluid in the core. Moreover, they considered limestone and dolomite as examples for the practical application of their method and simulated the permeability distribution of rocks well. Further, the finite volume method was proposed by Bijeljic et al. (2013). The lattice Boltzmann method is a widely used computational fluid dynamics method on the mesoscopic scale, and it has the characteristics of a mesoscopic model intermediate between a microscopic molecular dynamics model and a macroscopic continuous model. Therefore, it has the advantages of a simple description of fluid interaction, easy setting of complex boundaries, easy parallel computing, and easy implementation of the program (Degruyter et al. 2010). Sun et al. (2017) processed and used images of five carbonate rock samples obtained from 3D CT scans to calculate porosity and directional permeability. Subsamples taken at three positions along each original core plug image were processed to segmented images using image-processing methods. Porosities were calculated by the voxel statistics method based on a segmented image. The absolute permeabilities of these subsamples in the three main perpendicular directions were calculated by applying the parallel lattice Boltzmann method in our high-performance computing cluster. Hijaz et al. (2020) regarded 3D image visualization to be effective in characterizing the connectivity and continuity of thin sandstone layers

in heterolithic rocks. Using digital core technology, they proposed a method to improve the connectivity and permeability characterization of thin sandstone layers in heterolithic rocks. Florian et al. (2020) used irregular rock particles to model the digital core and focused on the mechanical characteristics of rock particles in the digital core, making it very helpful for us to analyze the separation of the core particles during displacement. Andrä et al. (2013) adopted a multiscale approach for gaining a deeper understanding of sand core microstructures as a standard for other material classes such as rocks. Tan et al. (2020) established a set of carbonate digital cores that contained fractures and calculated the elastic mechanical characteristics of the core based on the finite element method. Although the addition of fractures makes the digital core more accurate, thereby realizing more accurate calculation of reservoir oil and gas reserves, it does not consider the mineral composition and rock-particle size of the core. Therefore, fluid displacement experiments of the core cannot be performed. Nishank et al. (2019) He used mercury injection method, nuclear magnetic resonance and other indoor experimental methods to improve the digitization of digital core, in order to obtain more accurate core physical parameters.

Although researchers have constructed digital cores from different aspects, few studies have explored the use of digital cores, specially for indoor analysis experiments. From the perspective of oilfield development and production increase, this type of digital core is very important. Based on previous studies, a complete set of construction methods for digital cores used for indoor analysis experiments is proposed in this paper.

Construction of a digital core pore

CT scanning

When X-rays pass through a core sample, a series of complex physical phenomena, such as the electron-pair effect, Compton effect, and photoelectric effect, occur. Since the rays are partially reflected, scattered, and absorbed by the internal electrons of the core, the X-ray energy intensity is attenuated. The absorption coefficient of X-rays is related to the composition of core samples. Generally, the absorption of X-rays depends on the density of various components of the core. Therefore, the density of each part of the core can be determined by determining the X-ray absorption coefficient. X-rays produced by the X-ray generator irradiate the sample from different angles. The attenuated X-ray energy after passing through the sample was measured and recorded; the X-ray signal after attenuation was converted into an electrical signal and then into a digital image signal through an external sampling amplification and analog–digital conversion circuit. Finally, the absorption coefficient

corresponding to each layer of the sample was calculated to obtain a 3D image through computer processing.

Filter back-projection reconstruction was applied in this study. It is a widely used algorithm in CT image reconstruction and has high-resolution and high-reconstruction speed. The formula for the filtered back projection can be written as follows(Kiss et al. 2004):

$$f(x, y) = \int_0^\pi g(t, \theta)\mathrm{d}\theta \tag{1}$$

$$g(t, \theta) = \int_{-\infty}^{+\infty} P(\rho, \theta) \times |\rho| \times e^{2\pi j \rho t}\mathrm{d}\rho \tag{2}$$

The original image of the core and the condition of a section are shown in Fig. 1:

The results obtained after CT scanning and using the filtered back-projection reconstruction method are shown in Fig. 2.

Using these methods, a gray-scale map of the rock sample profile was obtained. It is seen that the generated profile reproduces the characteristics and details of the original rock sample well but also generates a lot of noise signals. Since the noise signals greatly affect the identification of pores, fractures, and lithology of rock samples, it is necessary to eliminate them.

Noise signal elimination

To eliminate the noise signal generated during scanning, the image should be filtered. For this purpose, the median filtering method is generally used. Median filtering is a nonlinear


Fig. 1 Overall morphology and profile morphology of the original rock

Fig. 2 Overall morphology and profile morphology after CT scanning

signal-processing method that can effectively suppress noise based on sorting statistics theory. The basic principle of this method is to scan the image to be processed with a template, and arrange all the pixels in the image covered by the template from large to small to take the value of the middle point of the sequence instead of the pixel value of the middle point of the window (taking a point as an example, its 26 neighborhoods are shown in Fig. 3). This method eliminates isolated noise points. Median filtering can not only remove noise, but also protect details of the image. Owing to the large number of pixels in a rock sample image, it is difficult to find the generated noise signal in the case of image shrinkage, and it is difficult to notice the effect of median filtering with the naked eye. However, in the digital process, to obtain accurate results, the noise signal must be eliminated. To show its effect, a section of a rock sample was used as an
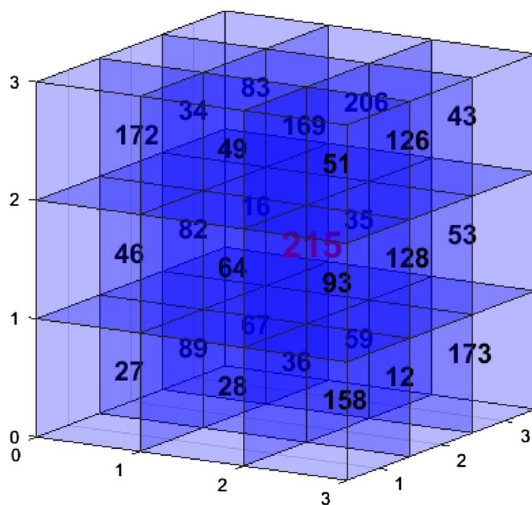
example, and some salt-and-pepper noise points were added so that the readers could clearly understand the effect of noise elimination. Figure 4 shows a section of the rock sample with more obvious noise signals, and noise elimination achieved after median filtering is presented in Table 1 and 2.

The gray value of the target point is 215, which changed to 64 after median filtering, demonstrating the good noise reduction performance (Figs. 5, 6, 7, 8, and 9).

The details of the rock sample profile were well preserved after median filtering, and the pore and fracture structures did not change, and the color was generally lighter. According to the principle of median filtering, to eliminate noise signal, the value of each point is changed to the mean value of itself and neighborhood. Hence, so the color of the rock sample part becomes lighter after median filtering processing—the gray value increases, indicating that the heterogeneity of rock sample increases, and the pore development is good. The gray values of part of the pores and cracks in the process of median filtering increase, and hence, the overall color of the rock sample becomes lighter Table. 3.

Threshold segmentation

After the noise signal of the rock sample is eliminated by the median filtering technology, it is necessary to identify the pores and fractures to construct the pores and fractures. Meanwhile, it is necessary to classify the extremely small part of the pores into one category and uniformly process them into the rock skeleton. The image-processing process mainly has the threshold segmentation method (Rosenfeld et al.1983; Ridler et al.1978; Otsu et al.1975), the cluster analysis method (Macoueen et al.1967; Abdi et al. 2007), and boundary detection method (Vincent et al.1991). The threshold segmentation method has the advantages of a simple algorithm, small amount of calculation, stable performance, and wide application. Further, this method is especially suitable for case of insufficient core samples, and hence, in this study, the threshold segmentation method was adopted to process the gray scale of rock samples. The maximum interclass variance method is a commonly used method in mathematics. In this study, this method was used for threshold segmentation. The principle of determining the segmentation threshold is that the set of gray values is divided into background and target groups ($T1$, $T2$) by
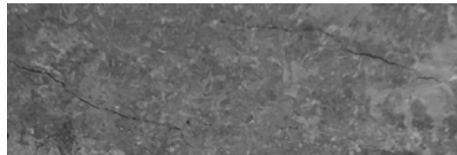

Fig. 3 Schematic diagram of 3D median filter
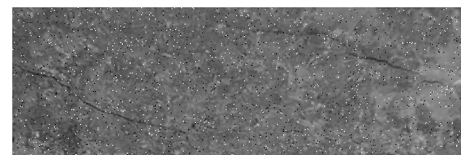
Fig. 4 Noise after adding salt-and-pepper noise signals in a section of the rock sample

Table 1 Original data of rock sample

27	89	67	28	36	59	158	12	173
46	82	16	64	215	35	93	128	53
182	34	83	49	169	206	51	126	43

Table 2 Data after median filtering

12	16	27	28	34	35	36	43	46
49	51	53	59	64	67	82	83	89
93	126	128	158	169	172	173	206	215

Fig. 5 Results of noise signal elimination by median filtering

Fig. 9 Threshold $T = 110$

Fig. 6 Threshold $T = 80$

Table 3 Classification of rock-particle size distribution

Mineral type	Calcite	Quartz	Montmorillonite
Particle size (μm)	60.7–(46.3%)	20.2–60.7 (34.6%)	5.6–20.2 (8.1%)
Mineral type	Kaolinite	Chlorite	Illite
Particle size (μm)	3.9–5.6 (4.7%)	2.5–3.9 (3.0%)	0–2.5 (3.3%)

Fig. 7 Threshold $T = 90$

threshold T. When the interclass variance of the two groups is the largest, the gray value T is the best threshold for image segmentation. The average gray level is calculated as follows:

$$gray = \omega_1 \times \overline{gray_1} + \omega_2 \times \overline{gray_2} \tag{3}$$

The interclass variance of the image is:

$$g(t) = \omega_1 \left(\overline{gray_1} - gray \right)^2 + \omega_2 \left(\overline{gray_2} - gray \right)^2 \tag{4}$$

The gray value T corresponding to the maximum variance interclasses is the threshold of optimal segmentation. This method is widely used and is the most classical method of global binarization. By changing the threshold and setting the partial transparency of the matrix as 100%, the obtained image segmentation results are as follows:
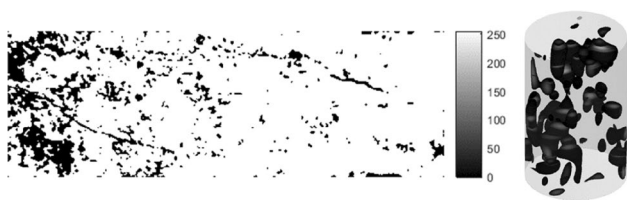

Fig. 8 Threshold $T = 100$

Fig. 10 Threshold $T = 92.1$

Fig. 11 Binary map of rock samples under the optimal threshold segmentation condition

According to the results, it can be seen that the change of threshold greatly affects the segmentation results of a rock sample image, and the selection of the threshold is crucial for the accuracy of the digital core. With an increase in the threshold, the matrix part of the rock sample is increasingly regarded as pores is more and more judged as pores. With a decrease in the threshold, an increasing number of pores of the rock sample are judged as the matrix. Whether the porosity is regarded as matrix or the matrix is regarded as porosity, the physical properties of the digital core are very different from the actual core. Therefore, the setting of the threshold should be just right. By calculating the interclass variance of the image, the threshold corresponding to the maximum value was found to be 92.1. The best segmentation result is shown in Fig. 10.

Under the optimal threshold segmentation conditions, the matrix part is displayed, and the overall segmentation results of rock samples are shown in Fig. 11.

The pore distribution of the core was numericalized by simple image processing. The real digital core also needs to improve some physical properties of the rock, such as the size of rock particles, rock mineral types, pore size distribution. In the previous literature, most of these physical properties of rocks are generated based on the random method. To obtain a more accurate and practical digital core, these physical characteristics were added to the numerical core based on the laboratory experiment.

Establishment of digital core lithology

Core lithology mainly includes mineral composition and content, particle-size distribution, and pore size distribution.

Mineral composition of the core

The core mainly comprises calcite, quartz, dolomite, syenite, plagioclase, metal minerals, etc. The core composition greatly determines the chemical reaction between the digital core and fluid, such as acid–rock reactions. The core also contains clay components, mainly illite, kaolinite, and montmorillonite, which determine the sensitivity of the digital core—for example, the water sensitivity, speed sensitivity, salt sensitivity, and alkali sensitivity.

The mineral composition of core was analyzed by using a DX-2700 X-ray diffractometer. The results are shown in Figs. 12 and 13:

The experimental results show that the total amount of calcium in rock samples is 46.3% ($CaCO_3$). Quartz is 34.6% (SiO_2), and clay is 19.1%. Among the clay minerals, kaolinite accounts for 24.5% ($Al_2Si_2O_5(OH)_4$); chlorite accounts for 15.6% ((Mg,Fe^{2+},Fe^{3+})$AlSi_3O_{10}(OH)_8$); illite accounts for 17.6% (($H_3,O,K)_y(Al_4 \cdot Fe_4 \cdot Mg_4 \cdot Mg_6)(Si_{8-y} \cdot Al_y)O_{20}(OH)_4$); and montmorillonite accounts for 42.3% (($Ca_{0.5}Na)_{0.7}(Al,Mg,Fe)_4(Si,Al)_8O_{20}(OH)_4 \cdot nH_2O$) (Figs. 14 and 15).

The core data after CT scanning can reflect the density of each point in the core. Hence, the CT scanning data were divided according to the proportion of each mineral component in the X-ray diffraction results of the core. The division method is as follows:

$$\begin{cases} N_{T_i} = \omega_{m_i} N & i = 1, 2, \dots n \\ \text{gray}_{T_i} = i \end{cases} \tag{5}$$

The results of core mineral composition modeling are shown in Fig. 16.

The distribution of rock minerals greatly influences the seepage of fluid in the core. The type and content of minerals will affect the pH of water—neutral or acidic in the core. Meanwhile, the distribution of rock particles was established based on the distribution of minerals.

Core pore size distribution

The pore size distribution of cores can be obtained by mercury intrusion experiments. Mercury can enter solid pores under external pressure. For the cylindrical pore model, the pore size and pressure of mercury can enter conform to the Washburn equation. By controlling different pressures, the volume of mercury can be measured,

Fig.12 Whole rock X-ray diffraction results
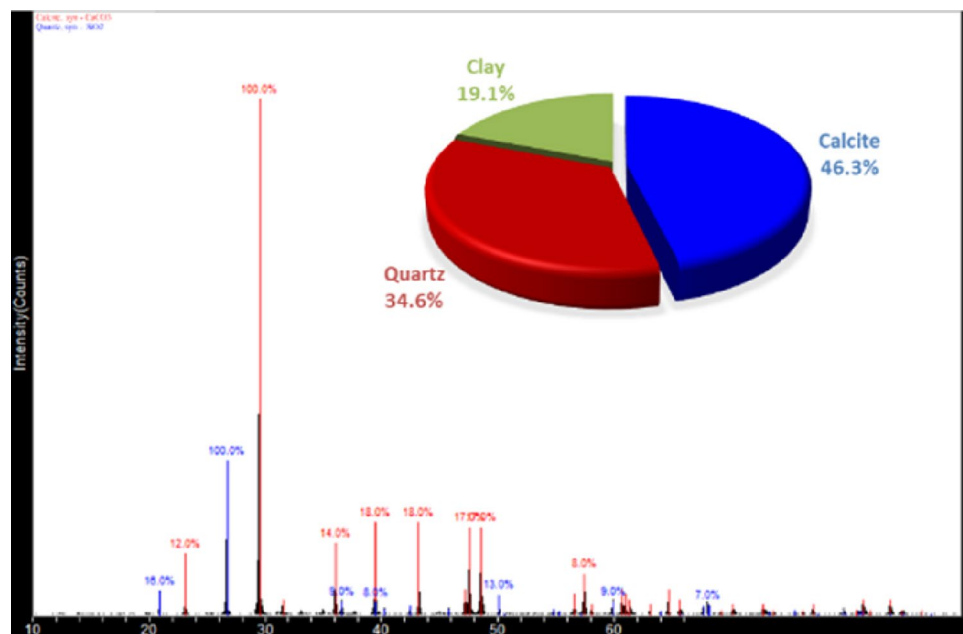
Fig.13 X-ray diffraction analysis results of clay
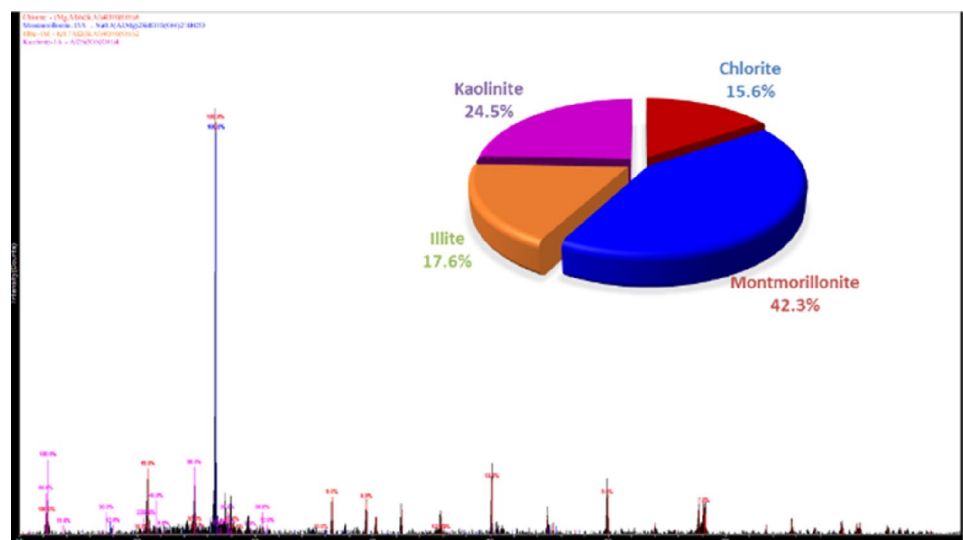
and the cumulative distribution pore size corresponding to different pressures can be obtained. The experimental results of mercury intrusion are shown in Fig. 17. The pore size distribution can be calculated by tracking the relation between the amount of mercury (nonwetting liquid) entering the pore and pressure. The pore size distribution of the core calculated by the Washburn equation is as follows:

$$R = \frac{-2\gamma \cos(\theta)}{\Delta P} \qquad (6)$$

Mercury injection and outflow data for rock samples are shown in Fig. 15. It can be seen that the displacement

pressure of the rock sample is small, and there are some large pores; when the mercury saturation is 50%, the injection pressure is too large, and the adjacent curve changes gently, which indicates that the pores of the rock sample are concentrated in the middle pores. The pore size distribution of the rock sample can be calculated by Eq. (6).

The pore size distribution measured by mercury intrusion curve can only simply describe the overall situation of the rock sample and cannot describe the distribution of pore size at each point of the rock sample. If the pore size is randomly assigned to each point of the rock sample, the pore size of the rock sample will have no spatial correlation. Meanwhile, if the abscissa of the above curve is changed to the particle size, and the ordinate is changed to the percentage of particle

Fig. 14 Mineral composition distribution of the core

Calcite(1)   Quartz(2)   Montmorillonite(3)   Kaolinite(4)   Chlorite(5)   Illite(6)
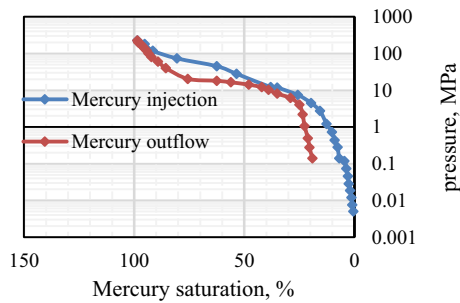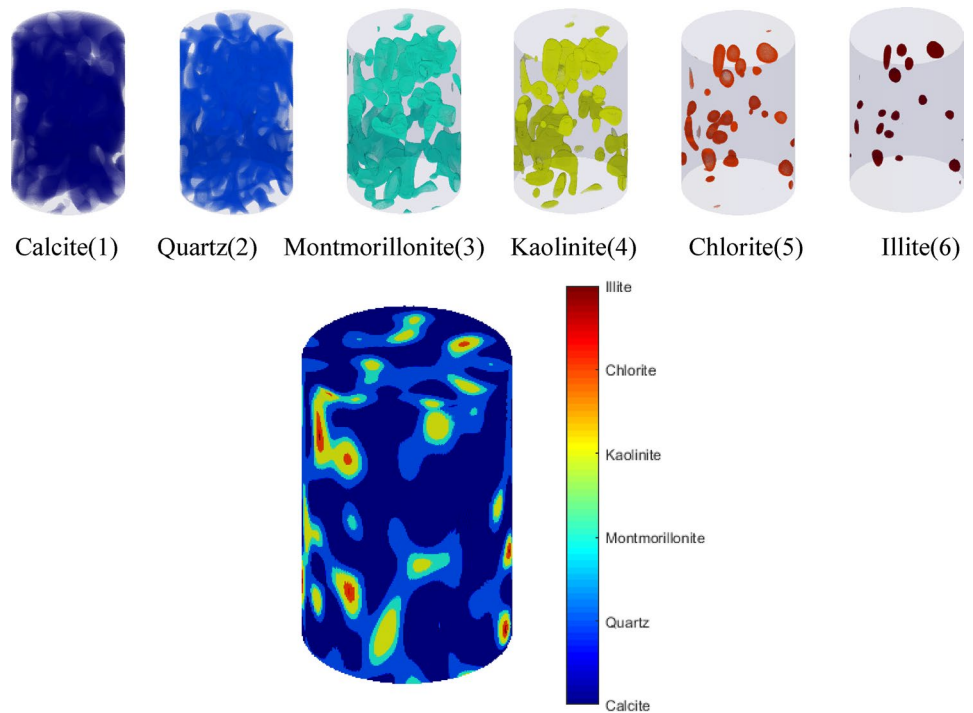
Fig. 15 Mercury injection and outflow data
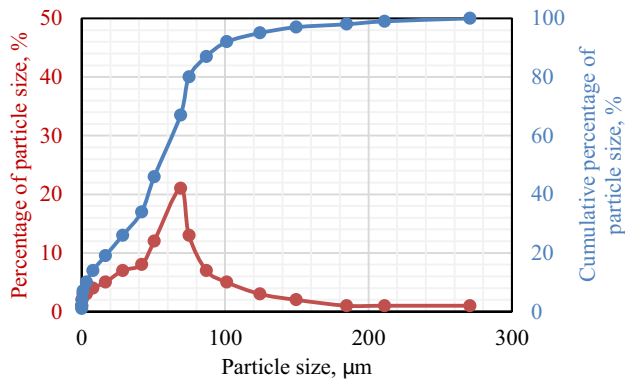
Fig. 16 Results of particle-size distribution is made measured by indoor test screening method

size, it is easy to get that the particle-size distribution of rock samples tends to normal distribution, then a pseudo-random pore size distribution model with spatial correlation can be established according to this property.

Since the number of pore size distribution obtained from mercury intrusion curve data is far less than the number of simulated grids, the data should be expanded by the interpolation method. Kriging interpolation method is based on the variation function and structure analysis and is a method of unbiased optimal estimation of regionalized variables in a finite region is very useful for constructing the pore size distribution with spatial correlation. Kriging interpolation method is expressed as follows:

$$R(x_0) = \sum_{i=1}^{n} \lambda_i R(x_i) \tag{7}$$

There is a certain correlation between $R(x_i)$, and this correlation and the distance, direction, and kriging interpolation were employed to meet unbiased, minimum variance conditions Eq. (8) (Li and Li, 2019):

$$\begin{cases} \sum_{i=1}^{n^*} \lambda_i C(x_i, x_j) + \mu = C(x_0, x_j)(j = 1, 2, \dots, n^*) \\ \sum_{i=1}^{n^*} \lambda_i = 1 \end{cases} \tag{8}$$

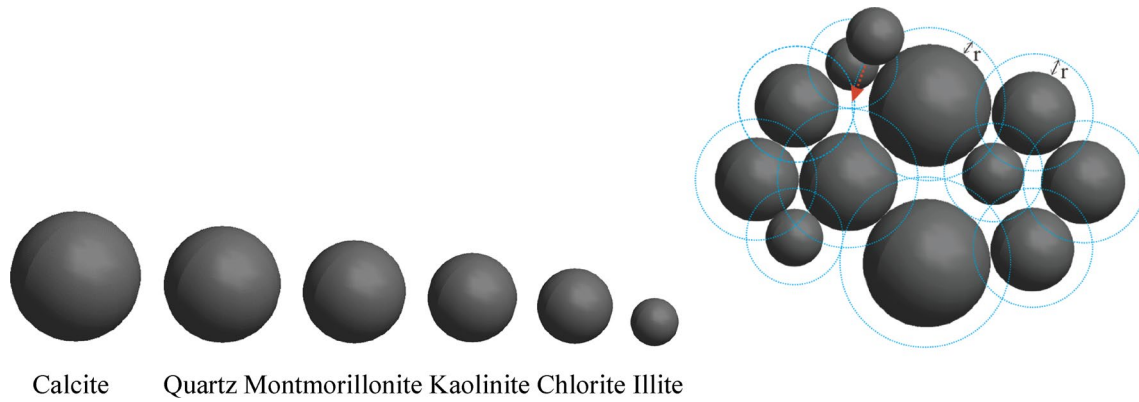$C(x_i, x_j)$ is the covariance function of $R(x_i)$ and $R(x_j)$.

Fig. 17 Regular rock-particle stacking

$$C(x_i, x_j) = \frac{1}{N(j-x)} \sum_{i=1}^{N(j-x)} \left[Z(x_i) - \overline{Z}(x_i) \right] \left[Z(x_j) - \overline{Z}(x_j) \right] \tag{9}$$

Thus, the aperture data with a low spatial correlation degree and a small number of data are interpolated into the aperture data with a high spatial correlation degree and large number of data, and the modeling of aperture distribution is realized.

Core particle-size distribution

The distribution of core particle size can be simply obtained by screening method. After the core is crushed, the rock powder is classified by using different mesh sieves. The results shown in Fig. 18 match the core particle size with mineral composition, and we can assume that the larger the density, the larger is the particle size. The matching method is as follows:

The maximum particle size corresponding to a core is as follows:

$$d_i = d|_{L_i = \sum_{i=1}^{n} \omega_{mi}} \tag{10}$$

The particle-size distribution of the core is as follows:

$$d_{P_i} = d_{i-1} - d_i \tag{11}$$

where the assumption is $d_0 = 0$, that is, the minimum particle size of the core approaches 0.

Ideally, rock particles are assumed as spheres. Under this assumption, the particle-size distribution of digital cores is constructed. For the arrangement of rock particles with different sizes, a novel method is proposed herein: the optimal contact descent method. If the radius of a particle that is about to sink is r, it is assumed that the radius of all settled particles increases by r. For example, in the part of the blue dotted line, the place where the dotted line sphere intersects the most is the place where the particle drops (descending coordinate).

$$\text{if} \left(\sqrt{(x_0 - x_i)^2 + (y_0 - y_i)^2 (z_0 - z_i)^2} - r - r_i \le 0 \right)$$
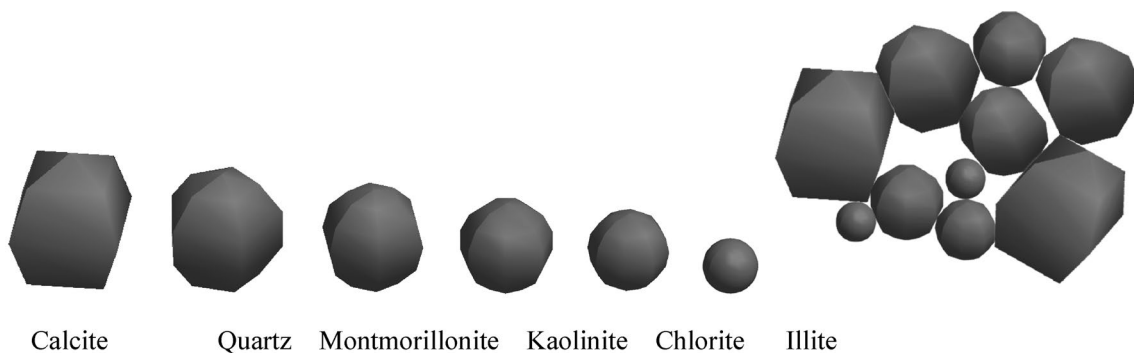
Then $h_i = 1, i = 1, 2, \cdots, n$

$$\tag{12}$$

Fig. 18 Particle stacking of irregular rocks

$$h_t|_{x=x_0,y=y_0,z=z_0} = \max\left(\sum_{i=1}^{n} h_i\right) \qquad (13)$$

If there are multiple optimal decline situations, they can be judged by calculating the sum of the distances from the decline point to each point in the neighborhood in each case. The smaller this value, the better is the arrangement of the particles is, namely, the final decline point.

$$\begin{cases} d_i = \sum_{i=1}^{n}\left(\sqrt{(x_0-x_i)^2+(y_0-y_i)^2+(z_0-z_i)^2}-r_i-r\right) \\ (r+r_i)^2 \le (x_0-x_i)^2+(y_0-y_i)^2+(z_0-z_i)^2, i=1,2,\cdots,n \end{cases}$$
$$\qquad (14)$$

$$d^*|_{x=x^*,y=y^*,z=z^*} = \min\left(d_i\right), i=1,2,\cdots,n \qquad (15)$$

The shape and arrangement of rock particles are shown in Fig. 17.

The rock particles are regarded as spheres for simple and fast calculation. However, extremely idealized assumptions will reduce the simulation accuracy. To closely reproduce the actual situation of the core, all core particles were not regarded spherical; the core is assumed as irregular polyhedrons (Fig. 19). The arrangement method is consistent with the sphere arrangement method; under this condition, the

arrangement method is only a better arrangement method but not the optimal arrangement method. The optimal arrangement method is restricted by the algorithm and computer performance, and the resultant shape is difficult to obtain:

In theory, the arrangement of irregular polyhedron will make the contact area between the rock particles larger, more closely arranged, and the macroscopic performance is that the rock sample is more tight, the heterogeneity is stronger, and However, it also brings some problems, and the calculation of porosity and permeability of rock samples becomes very complex. The results of digital core modeling are as follows:

At the same time, this paper assumes that the rock particles of the same rock correspond to the same particle shape, and the arrangement is unchanged, as shown in Fig. 20. Of course, this method may not be used, but the different shapes of particles are randomly distributed according to particle-size distribution.

According to the method adopted in this study, the final digital core modeling results are as Fig. 21, the core of the local amplification, you can see the rock particles arranged in disorder together.

Thus, the pore structure of the digital core with lithology was established. To verify the accuracy of the model, the rock porosity attribute will be used to verify the model.

Fig. 19 Digital core model

(a) spherical particles   **(b)** irregular polyhedron particles

Fig. 20 Irregular rock-particle shape and mineral type

Calcite   Quartz   Montmorillonite   Kaolinite   Chlorite   Illite

(a) spherical rock particles   **(b)** irregular polyhedron-shaped rock particles
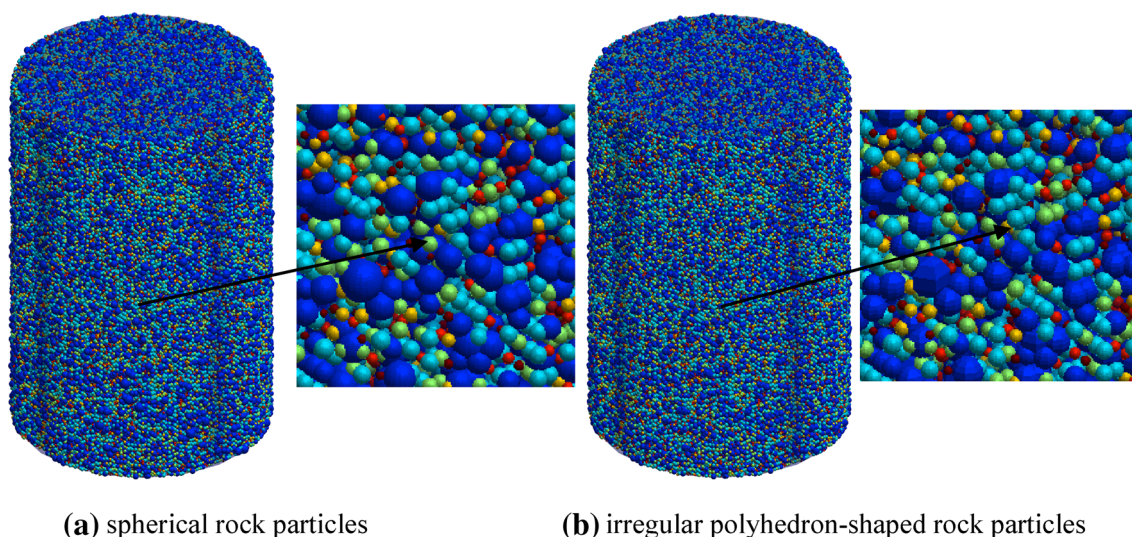
Fig. 21 Digital core model

Model verification

Using the digital core pore structure established in this study, the core model was validated based on rock porosity. Model porosity was calculated as follows:

$$\phi = \frac{1 - V_p}{V_{\text{rock}}} \tag{16}$$

$$V_p = \sum_{i=1}^{n^*} V_{p_i} \tag{17}$$

$$r^* = \left(\frac{V_{p_i}}{\pi}\right)^{1/3} \tag{18}$$

The particle volume of an irregular polyhedron $\left(V_{p_i}\right)$ can be directly obtained using MATLAB. The porosity of rock obtained by computer is 32.4%, and the porosity calculated by laboratory nuclear magnetic resonance method is 29.9%, as shown in Fig. 22, with high coincidence, which verifies the accuracy of the model. Correlating the change in porosity with the physical and chemical changes of particles is difficult. During water flooding, part of the clay minerals in the core will swell—the most obvious swelling is observed in the case of montmorillonite—characterized by the increase in rock-particle volume. Meanwhile, during acid flooding, part of the minerals in the core (the hydrochloric acid system will dissolve calcite; the soil acid system will dissolve quartz, clay, etc.), making the rock particle decrease. For an increase or a decrease in rock-particle volume, it is difficult to describe these changes via
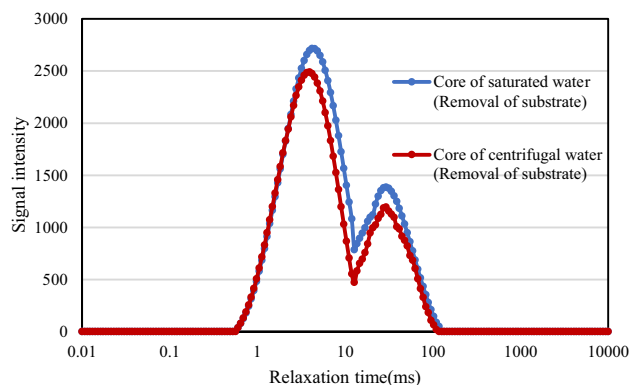
Fig. 22 Nuclear magnetic resonance results of rock sample

a mathematical expression when the irregular polyhedron shape is assumed. Therefore, in this study, the equivalent radius method was used to characterize the change of a rock-particle volume. This assumption method does not affect the seepage state of fluid in rock. Thus, researchers can conduct subsequent simulation of fluid flow in the core.

Conclusion

Digital cores based on laboratory experiments are usually more realistic and accurate than those generated by random algorithms. The CT scanning technology, X-ray diffraction technology, mercury intrusion experiment, and screening method can well characterize the physical properties of the core. In this study, CT scanning and filter back projection

were used to visualize the core. Further, 3D median filtering technology was used to eliminate the noise signal after scanning. The maximum interclass variance method was used to segment the rock structure and pores. X-ray diffraction technology was used to qualitatively and quantitatively distinguish the minerals in the core and realize their distribution in the core. The core pore size distribution was analyzed by mercury intrusion, and the core pore size distribution with spatial correlation was constructed by kriging interpolation. The particle-size distribution of the cores was analyzed by the screening method, and the rock-particle shape was assumed to be a more realistic irregular polyhedron. Considering the particle shape and mineral distribution together, the pore structure of the digital cores and the establishment of cores were realized. The simulated digital core porosity was 32.4%, and the core porosity measured by nuclear magnetic resonance experiment was 29.9%, with a high consistency, thereby validating the accuracy of the model. A method for simulating physical and chemical changes in subsequent digital cores was proposed to facilitate further study of this method.

References

Abdi H (2007) Discriminant correspondence analysis. Encyclopedia of measurement and statistics. Sage, Thousand Oaks (CA), pp 1–10

Al-Fatlawi O, Hossain MM, Saeedi A (2017) A new practical method for predicting equivalent drainage area of well in tight gas reservoirs. In: SPE Europec featured at 79th EAGE conference and exhibition. Society of Petroleum Engineers

Andrä H, Combaret N, Dvorkin J, Glatt E, Han J, Kabel M, Keehm Y, Krzikalla F, Lee M, Madonna C, Marsh M, Mukerji T, Saenger EH, Sain R, Saxena N, Ricker S, Wiegmann A, Zhan X (2013) Digital rock physics benchmarks—part I: imaging and segmentation. Comput Geosci 50:25–32. https://doi.org/10.1016/j.cageo.2012.09.005

Arns CH, Knackstedt MA, Pinczewski WV, Garboczi EJ (2002) Computation of linear elastic properties from microtomographic images: methodology and agreement between theory and experiment. Geophysics 67(5):1396–1405

Bijeljic B, Mostaghimi P, Blunt MJ (2013) Insights in to non-Fickian solute transport in carbonates. Water Resour Res 49(5):2714–2728. https://doi.org/10.1002/wrcr.20238

Degruyter W, Burgisser A, Bachmann O, Malaspinas O (2010) Synchrotron X-ray microtomography and lattice Boltzmann simulations of gas flow through volcanic pumices. Geosph Geol Soc Am 6:470–471

Dvorkin J, Derzhi N, Qian F, Nur A (2009) From micro to reservoir scale: permeability from digital experiments. Lead Edge 28(12):1446–1452

Ettemeyer F, Lechner P, Hofmann T, Andrä H, Schneider M, Grund D, Volk W, Günther D (2020) Digital sand core physics: Predicting physical properties of sand cores by simulations on digital microstructures. Int J Solids Struct 188–189:155–168. https://doi.org/10.1016/j.ijsolstr.2019.09.014

Fu L, Liao K, Ge J, Huang W, Chen L, Sun X, Zhang S (2020) Study on the damage and control method of fracturing fluid to tight reservoir matrix. J Nat Gas Sci Eng 82:103464

Hasnan HK, Sheppard A, Hassan MHA, Knackstedt M, Abdullah WH (2020) Digital core analysis: improved connectivity and permeability characterization of thin sandstone layers in heterolithic rocks. Mar Pet Geol 120:104549. https://doi.org/10.1016/j.marpetgeo.2020.104549

Kalam Z, Gibrata M, Hammadi MA, Mock A, Lopez O (2013) Validation of digital rock physics based water-oil capillary pressure and saturation exponents in super giant carbonates reservoirs. In: SPE-164413-MS. presented at the SPE middle east oil and gas show and conference held in manama, Bahrain, 10–13 March

Karimpouli S, Faraji A, Balcewicz M, Saenger EH (2020) Computing heterogeneous core sample velocity using digital rock physics: a multiscale approach. Comput Geosci 135:104378. https://doi.org/10.1016/j.cageo.2019.104378

Kiss T, Adam P, Janszky J (2004) Gauss filtered back projection for the reconstruction of the Wigner function. Acta Phys Hung B 20:47–50. https://doi.org/10.1556/APH.20.2004.1-2.10

Küntz M, Mareschal JC, Lavallé EP (2000) Numerical estimation of electrical conductivity in saturated porous medium with a 2-D lattice gas. Geophysics 65(3):766–772

Li X, Li S (2019) A meshless projection iterative method for nonlinear Signorini problems using the moving Kriging interpolation. Eng Anal Bound Elem 98:243–252. https://doi.org/10.1016/j.enganabound.2018.10.025

Macoueen J (1967) Some methods for classification and analysis of multivariate observations. In: Proceedings of the fifth Berkeley symposium on mathematical statistics and probability, vol 1. pp 281–297

Mostaghimi P, Blunt MJ, Bijeljic B (2012) Computations of absolute permeability on micro-CT images. Math Geosci 45(1):103–125

Otsu NA (1975) Threshold selection method from gray-level histograms. Automatica 11:23–27

Ridler TW, Calvard S (1978) Picture thresholding using an iterative selection method. IEEE Trans Syst Man Cybern 8(8):630–632

Riepe L, Suhaimi MH, Kumar M, Knackstedt MA (2011) Application of high resolution Micro-CT imaging and pore network modeling (PNM) for the petrophysical characterization of tight gas reservoirs-a case history from a deep clastic tight gas reservoir in Oman. SPE-142472-PP. In: Presented at the SPE middle east unconventional gas conference and exhibition held in Muscat, Oman

Rosenfeld A, De La Torre P (1983) Histogram concavity analysis as an aid in threshold selection. IEEE Trans Syst Man Cybern 2:231–235

Sadeq D, Iglauer S, Lebedev M, Rahman T, Zhang Y, Barifcani A (2018) Experimental pore-scale analysis of carbon dioxide hydrate in sandstone via X-Ray micro-computed tomography. Int J Greenh Gas Control 79:73–82

Saenger EH, Krüger OS, Shapiro SA (2004) Effective elastic properties of randomly fractured soils: 3D numerical experiments. Geophys Prospect 52(3):183–195. https://doi.org/10.1111/j.1365-2478.2004.00407.x

Saxena N, Hows A, Hofmann R, Alpak FO, Dietderich J, Appel M, Freeman J, De Jong H (2019) Rock properties from micro-CT images: digital rock transforms for resolution, pore volume, and field of view. Adv Water Resour 134:103419. https://doi.org/10.1016/j.advwatres.2019.103419

Schembre JM, Kovscek AR (2003) A technique for measuring two-phase relative permeability in porous media via X-ray CT measurements. J Petrol Sci Eng 39(1–2):159–174. https://doi.org/10.1016/S0920-4105(03)00046-9

Shabro V, Torres-Verdin C, Javadpour F, Sepehrnoori K (2012) Finite-difference approximation for fluid-flow simulation and calculation of permeability in porous media. Transp Porous Media 94:775–793. https://doi.org/10.1007/s11242-012-0024-y

Sun H, Vega S, Tao G (2017) Analysis of heterogeneity and permeability anisotropy in carbonate rock samples using digital rock physics. J Pet Sci Eng 156:419–429. https://doi.org/10.1016/j.petrol.2017.06.002

Tan M, Mengning Su, Liu W, Song X, Wang S (2020) Digital core construction of fractured carbonate rocks and pore-scale analysis of acoustic properties. J Pet Sci Eng 196:107771. https://doi.org/10.1016/j.petrol.2020.107771

Taud H, Martinez-Angeles R, Parrot JF, Hernandez-Escobedo L (2005) Porosity estimation method by X-ray computed tomography. J Pet Sci Eng 47(3–4):209–217. https://doi.org/10.1016/j.petrol.2005.03.009

Vincent L, Soille P (1991) Watersheds in digital spaces: an efficient algorithm based on immersion simulations. IEEE Trans Pattern Anal Mach Intelle 13(6):583–659

Wan R (2011) Advanced well completion engineering. Gulf professional publishing, Texas